Title	Novel Kinematic Model of a SCARA-type Robot with Bi-directional Angular Positioning Deviation of Rotary Axes
Author(s)	Zhao, Nan; Ibaraki, Soichi
Citation	The International Journal of Advanced Manufacturing Technology , 120 : 4901 - 4915
Issue Date	2022-03-23
DOI	
Self DOI	
URL	https://ir.lib.hiroshima-u.ac.jp/00054003
Right	This version of the article has been accepted for publication, after peer review (when applicable) and is subject to Springer Nature's AM terms of use, but is not the Version of Record and does not reflect post-acceptance improvements, or any corrections. The Version of Record is available online at: https://doi.org/10.1007/s00170-022-08943-5 この論文は出版社版ではありません。引用の際には出版社版をご確認、ご利用ください。
Relation	

Novel Kinematic Model of a SCARA-type Robot with Bi-directional Angular Positioning Deviation of Rotary Axes

Nan Zhao[1] and Soichi Ibaraki[2*]

[1]School of Engineering, The University of Tokyo, 4-6-1 Komaba, Meguro-ku, 153-8505, Tokyo, Japan.

[2*]Graduate School of Advanced Science and Engineering, Hiroshima University, 1-3-2 Kagamiyama, Higashi-Hiroshima, 739-8511, Hiroshima, Japan.

*Corresponding author(s). E-mail(s): Ibaraki@hiroshima-u.ac.jp;
Contributing authors: Nanzhao@g.ecc.u-tokyo.ac.jp;

Abstract

This paper proposed a kinematic model and its calibration scheme to further improve an industrial robot's absolute positioning accuracy over the entire workspace. To demonstrate the proposed model and its effectiveness in simplified kinematics, this paper only targets a SCARA (Selective Compliance Assembly Robot Arm) -type robot. The proposed model includes not only link length errors and rotary axis angular offsets, widely known as the Denavit-Hartenberg (D-H) parameters, but also the "error map" of the angular positioning deviation of each rotary axis, modelled as a function of command angular position, and the rotation direction to model the influence of backlash. The angular positioning deviation of each rotary axis is identified by measuring the robot's end-effector position by a laser tracker with indexing each rotary axis at prescribed angular positions. To verify the validity of the identified model, the effectiveness of the compensation based on it is experimentally investigated. By the compensation, the robot's average absolute position error was reduced by 33% to 0.034mm. Furthermore, this paper experimentally demonstrates that the proposed model can be extended to the radial error motion, axis-to-axis cross talk, and the three-dimensional positioning with orientation errors of axis average lines.

Keywords: Calibration, Compensation, Kinematic model, Industrial robot.

1 Introduction

1.1 Background

An industrial robot is usually programmed by the teach-in method, where a human operates the robot manually by using a teach pendant, and the robot memorizes it. Since the operator's command trajectory may or may not be optimal, the "absolute" positioning accuracy is typically not regarded as crucial for robots [1]. When a robot has sufficiently high positioning repeatability, the operator can modify its motion manually to successfully perform the required task. In this paper, the "absolute" positioning error represents the relative deviations between the actual and ideal position of the robot's end effector in X-, Y- and Z-directions [2]. On the other hand, a CNC (computer numerical control) machine tool is typically programmed by the CAM (computer-aided manufacturing) programming software based on a 3D (three-dimensional) model of the workpiece. In such programming, the command trajectory is calculated from the workpiece geometry to be finished, and the machine's "absolute" positioning accuracy determines the finished workpiece's geometric accuracy. In today's market, more users require a robot to have higher absolute positioning accuracy due to, e.g. the need for reducing the time and the cost with the teach-in operations. To program a robot based on a 3D model of its working environment ("offline programming"), higher absolute positioning accuracy may be critically required to successfully perform the given task.

Furthermore, higher absolute positioning accuracy may be a key to further extending a robot's applications. For example, many researchers and engineers study robotic machining as a viable alternative to machine tools especially for a large part due to its portability and lower implementation cost [3–5]. For machining operations with complex tool paths, the teach-in programming and manual modification of the robot's motion are no longer possible. The application of a robot to the 3D printing [6], [7] and 3D scanning [8] can also benefit from the improvement of a robot's absolute positioning accuracy.

1.2 Prior Art

To improve the absolute positioning accuracy of an industrial robot, the majority of past works target the identification of the D-H (Denavit-Hartenberg) parameters in the robot kinematics. The D-H parameters represent position and orientation errors of the axis average line of each rotary axis in a local coordinate system defined with respect to another axis. ISO 230-1 [2], the international standard on machine tool accuracy tests, defines the term, the *axis average line* of a rotary axis, as a straight line representing the mean position and orientation of the axis of rotation over the full rotation. For machine tools, ISO 230-7 [9] describes the test procedures to measure position and orientation errors of rotary axis average lines. For robots, many researchers proposed a scheme to identify the D-H parameters from the measurement of the end effector position. For easier and lower-cost measurement, some researchers presented the measurement of the end effector position when it is nominally constrained at a point [10], [11], on a line [12], on a spherical surface [13, 14], or on a plane [15]. Recently, more researches employ either a laser tracker [16, 17] or a vision-based measurement system [18–20], which can measure the end effector's 3D position at arbitrary positions over the entire workspace.

It should be emphasized that the axis average line only represents the *mean* position/orientation of the axis of rotation. The axis of rotation may be displaced in the radial or axial direction, or tilted, during its rotation. These error motions are referred to as radial, axial and tilt error motions in ISO 230-7 [9]. The *error motion* of a rotary axis is the term defined in ISO 230-1 [2] and represents changes in position and orientation of axis of rotation relative to its axis average line as a function of angle of rotation of the rotary axis.

The *angular positioning error motion* can be also a major error source, which cannot be described by the D-H parameters. The angular positioning error motion, also defined in ISO 230-1 [2], represents the actual angular position reached by the rotary axis minus the commanded angular position in the plane perpendicular to the axis average line. A robot's rotary axis is often driven via a power transmission mechanism such as a timing belt, a plenary gear, and a strain wave gear. The pitch error of such a gear causes the angular positioning error motion of each rotary axis. The angular positioning deviation generally varies with the command angular position, due to tooth-to-tooth variation in the gear pitch error. On the other hand, position and orientation errors of the axis average line are constant regardless of the axis' angular position. Some researchers call them position-independent errors [21].

A robot's rotary axis also has error motions, and they are, predictably, often larger than those in machine tools. In a robot's rotary axis, a rotary encoder is often installed on the motor axis only, i.e. no encoder for the actual axis of rotation [22]. This increases the influence of the gear pitch error on the angular positioning error motion. Furthermore, the gear transmission mechanism often has the backlash, resulting in the bidirectional angular positioning deviation. The influence of the angular positioning error motion on the positioning error at the robot's end effect becomes larger in proportion to the distance from it to the axis of rotation. Unlike, e.g. a rotary table for a machine tool, it is inherently difficult for a robot to keep this distance shorter. As a result, for robots, the angular positioning deviation of rotary axes often gives a significantly larger influence on the positioning accuracy at the end effector than for machine tools.

Some past studies report that even when the influence of the D-H parameters are compensated, the positioning error of the robot is still roughly 10 to 100 times larger than that of a typical machine tool [23–25](Refs. [23, 24] review the achieved positioning accuracy from total 20 papers for various robots including six-axis robots. Ref. [25] focuses on the geometric calibration of SCARA robots). To compensate for error motions in addition to the D-H parameters, some researches have modelled the error in a non-geometric way, typically by the neural network model [26, 27]. To ensure compensation performance over the entire workspace, geometric model-based approaches are

more promising. Some works discussed the influence of joint compliance and friction [28, 29]. Some recent works have measured and modelled rotary axis angular positioning error motion. For a 6-DoF (degrees of freedom) robot, Nubiola et al. [16] presented the measurement of the angular positioning error motion of each rotary axis by using a laser tracker. Hörler et al. [30] measured the angular positioning deviation of two rotary axes in a SCARA (Selective Compliance Assembly Robot Arm) -type robot and modelled it as a function of command angular position. They also measured the backlash (hysteresis) of each axis but its inclusion into the kinematic model was not clearly presented in [30].

This paper considers the static modeling of robot kinematics for the feedforward modification of command trajectories. Optimal design of feedback controllers for motors, with the dynamic modeling of a robot and the influence of external forces, can also contribute significantly to a robot's positioning accuracy [31, 32]. Many researchers have presented a feedback control based on an additional position measurement, such as the joint-side angular position measurement (secondary encoder) [33] and direct measurement of end effector position by using a laser tracker [34]. This paper does not involve the feedback control but focuses on the robot kinematic errors that cannot be observed by an encoder.

1.3 Contribution

To predict the robot's positioning accuracy in higher accuracy than the conventional kinematic model with the D-H parameters only, this paper proposes a new kinematic model with the bidirectional angular deviation of each rotary axis, in addition to the D-H parameters. One of the essential differences between machine tools and robots is the difficulty indirect measurement of rotary axis error motions. For example, the angular positioning error motion of a rotary table in a five-axis machine tool is typically measured by using an autocollimator with a reference polygon mirror or a reference indexing table (ISO 230-1 [2]). For a robot, such a measurement is difficult, since a reference polygon mirror or a reference indexing table must be placed on the axis of rotation, which requires a special fixture. This paper proposes the application of a laser tracker to indirectly estimate the angular positioning deviation from the measurement of the end effector positions.

The proposed model of a SCARA-type robot with the position-dependent, direction-dependent angular positioning deviations was first proposed by the authors' group in [35]. Compare to [35], this paper's original contributions are as follows: a) In Ref. [35], angular positioning deviations are identified by a special measurement scheme. This paper presents a more generally applicable measurement scheme using a commercial laser tracker, at the expense of the instrument's higher cost. b) numerical compensation based on the proposed model is first presented in this paper, and c) the extension of the present model is presented to include the following potential error sources: the radial error motion, the axis-to-axis cross talk, and the orientation errors of axis average lines to model the 3D positioning error. A laser tracker is employed in some recent works in the literature but its application to the identification of position-dependent error motions is a part of this paper's original contributions.

1.4 Limitation

To investigate the effectiveness of the proposed model in a simpler kinematics, this paper only presents the application to 2D positioning by the SCARA-type robot. A SCARA-type robot is usually not for the applications requiring higher rigidity, and we do not intend to apply a SCARA-type robot to machining operations. The application to a SCARA-type robot is studied to investigate the fundamental validity and performance of this new methodology. Our final goal is to apply the present model to a 6-DoF robot, which will be studied in our future research.

A change in the robot kinematics can result in the deterioration of the positioning accuracy for any feedforward, model-based compensation schemes. Such a change can be caused by, for example, environmental influences, including temperature change, an external load to the robot, and the gear wear. This paper does not study such an influence. In particular, our group [36] has shown thermal influence can significantly influence the positioning accuracy of a SCARA robot, and presented a scheme to measure it.
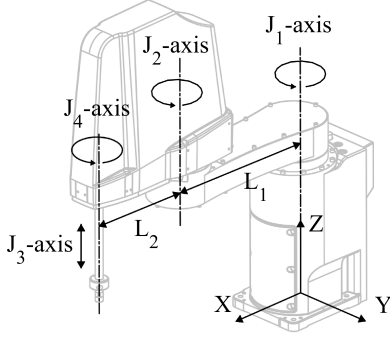
Fig. 1: The SCARA-type robot configuration

2 Proposed model and its identification scheme

2.1 Conventional kinematic model with the D-H parameters

The geometric configuration of the SCARA-type robot considered in this paper is shown in Fig. 1. When the robot without geometric error, the k-th end effector position in the reference coordinate system (CS), $P^*(k) \in \mathbb{R}^3$, is formulated by the nominal forward kinematic model as Eq. (1).

$$P^*(k) = \begin{bmatrix} L_1 \cos{(\theta_1^*(k))} + L_2 \cos{(\theta_1^*(k) + \theta_2^*(k))} \\ L_1 \sin{(\theta_1^*(k))} + L_2 \sin{(\theta_1^*(k) + \theta_2^*(k))} \\ Z^*(k) \end{bmatrix} \tag{1}$$

where k is the index number of the command position, $k = 1, \ldots, N$, and N is the number of command positions. L_1 and L_2 are link one and link two lengths of the SCARA-type robot (see Fig. 1), $\theta_1^*(k)$ and $\theta_2^*(k)$ are the commanded angular positions of J_1- and J_2-axis, $Z^*(k)$ is the commanded Z-position in the reference CS. The superscript "*" represents commanded values throughout this paper. The posture shown in Fig. 1 is at $\theta_1^*(k) = \theta_2^*(k) = 0$. The reference CS is the fixed CS with its Z-axis aligned to the J_1-axis of rotation (see Fig. 2). The Z-position of its origin can be set arbitrary.

To study the fundamental validity of the proposed scheme in the simplified problem, this paper basically considers the 2D positioning error on the XY plane only; the positioning error in the Z-direction will be studied only in Section 5.3.

As reviewed in Section 1, the majority of the previous works on error calibration for industrial robot are based on the kinematic model with the D-H parameters. For the SCARA-type robot in

Fig. 1, when only the 2D positioning error is considered, the D-H parameters are: the link length errors, denoted by $\triangle L_1$ and $\triangle L_2$, and the angular offset with J_2-axis, denoted by θ_{20}. With these D-H parameters, the 2D end effector position in Eq. (1) can be rewritten by Eq. (2).

$$\hat{P}_{\text{con}}(k) = \begin{bmatrix} \cos{(\theta_1^*(k))} & \cos{(\theta_1^*(k) + \theta_2^*(k) + \theta_{20})} \\ \sin{(\theta_1^*(k))} & \sin{(\theta_1^*(k) + \theta_2^*(k) + \theta_{20})} \end{bmatrix} \begin{bmatrix} L_1 + \Delta L_1 \\ L_2 + \Delta L_2 \end{bmatrix} \tag{2}$$

The variables with "ˆ" represent estimated values throughout this paper.

ISO 230-7 [9] describes that a single rotary axis has six error motions, as well as four errors representing the position and orientation of its axis average line. The angular positioning error, included in the proposed model, is one of six error motions. While Sections 2−4 only consider the 2D positioning, this paper also presents the proposed model's extension to the 3D positioning in Section 5. The radial error motion, to be presented in Section 5.1, is another error motion, and further extension to another four error motions would be straightforward.

The angular error motions (yaw, pitch and roll) of the end effector are not considered in this paper. A laser tracker, with a single retroreflector, measures the retroreflector position only. When the end effector orientations can be measured, the extension of the present model to angular error motions is potentially possible, but it is out of this paper's scope.

2.2 Proposed kinematic model

The major contribution of this paper is in the proposal of a new kinematic model with rotary axis angular positioning deviations, in addition to the conventional D-H parameters. As was discussed in Section 1, the angular positioning deviation of a rotary axis is typically caused by the gear pitch error. To model its influence, in the proposed model, the angular positioning deviation is a function of the command angular position. Furthermore, since a robot's rotary axis is often subject to significant influence of the gear backlash, different angular positioning deviation should be assigned for different rotation direction.

For the command angular position of the J_n-axis $(n = 1, 2)$, $\theta_{n,\text{map}}^*(i_n)$, where $i_n = 1, \ldots, N_n$ is

the index number, the angular positioning deviation is denoted by $\Delta\theta^*_{n,\text{map}}(i_n, \text{sgn}(\dot{\theta}^*(i_n)))$. It is a function of the command angular position, represented by the index number i_n, and furthermore, a function of the rotation direction, $\text{sgn}(\dot{\theta}^*_n(i_n))$, where $\text{sgn}(\dot{\theta}^*_n(i_n))$ is assigned a value of $+1$ (or -1) when $\dot{\theta}^*_n(i_n) > 0$ (or $\dot{\theta}^*_n(i_n) < 0$), $\dot{\theta}^*_n(i_n)$ represents the angular velocity of J_n-axis at $\theta^*_n(i_n)$. When the command J_n-axis angular position $(n = 1, 2)$ is given arbitrarily by $\theta^*_n(k)$, the proposed kinematic model is given by Eq. (3).

$$\hat{P}(k) =$$
$$\begin{bmatrix} \cos(\hat{\theta}_1(k)) & \cos(\hat{\theta}_1(k)+\hat{\theta}_2(k)+\theta_{20}) \\ \sin(\hat{\theta}_1(k)) & \sin(\hat{\theta}_1(k)+\hat{\theta}_2(k)+\theta_{20}) \end{bmatrix} \begin{bmatrix} L_1+\Delta L_1 \\ L_2+\Delta L_2 \end{bmatrix}$$
$$(3)$$

where $\hat{\theta}_n(k)$ is the estimated angular position of the J_n-axis, and is given by linearly interpolating $\Delta\theta^*_{n,\text{map}}(i_n, \text{sgn}(\dot{\theta}^*_n(i_n)))$ $(n = 1, 2)$ as Eq. (4).

$$\hat{\theta}_n(k) = \theta^*_n(k) + \delta_n(k) \cdot \Delta\theta^*_{n,\text{map}}(i_n, \text{sgn}(\dot{\theta}^*_n(k)))$$
$$+ (1 - \delta_n(k)) \cdot \Delta\theta^*_{n,\text{map}}(i_n + 1, \text{sgn}(\dot{\theta}^*_n(k))) \quad (4)$$

and i_n $(n = 1, 2)$ must meet:

$$\theta^*_{n,\text{map}}(i_n) \leq \theta^*_n(k) \leq \theta^*_{n,\text{map}}(i_n + 1) \quad (5)$$

$\delta_n(k)$ $(n = 1, 2)$ are the interpolation weights, given by Eq. (6).

$$\delta_n(k) = \frac{\theta^*_n(k) - \theta^*_{n,\text{map}}(i_n)}{\theta^*_{n,\text{map}}(i_n + 1) - \theta^*_{n,\text{map}}(i_n)} \quad (6)$$

Remark 1: In the proposed kinematics model (Eq. (3)), the angular offset of J_1-axis is not considered, because the reference CS is defined according to the direction of the Link 1 when J_1-axis is indexed at $\theta_1^* = 0$. The angular offset of J_1-axis is needed if the reference CS is defined in the prescribed direction. This is the case, for example, when there exists a reference hole or slot on a work table to define the direction of the reference CS.

Remark 2: The D-H model in [37] defines four parameters, namely the link twist angle, the link length, the joint distance and the joint angle, for each CS aligned to the axis average line. The present model (3) is essentially equivalent to the D-H model, but it represents the XY position only, which eliminates the influence of the link twist and

(a) J_2-axis indexing test

(b) J_1-axis indexing test
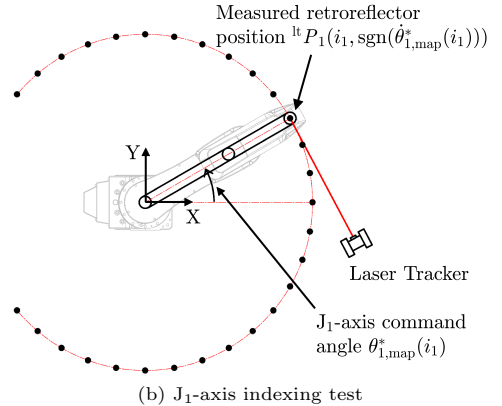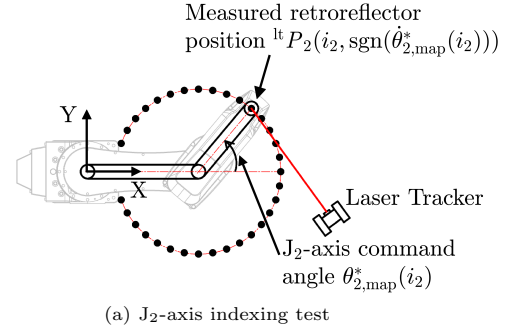
Fig. 2: Measurement procedure
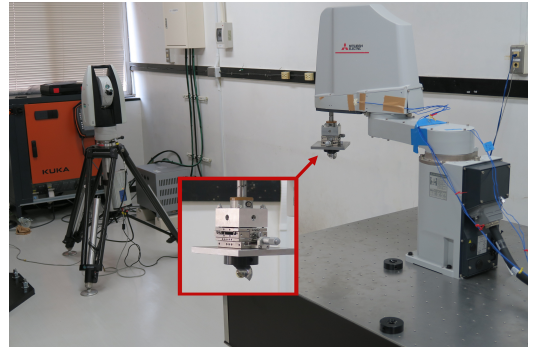
Fig. 3: Experimental setup with laser tracker and robot

joint angles. The parallelism errors investigated in Section 5.3 correspond to the link twist and joint angles. Alam et al. [38] discussed the formulation of various equivalent D-H models from different CS definitions.

2.3 Proposed measurement procedure

Another original contribution of this paper is on the proposal of a scheme to identify all the parameters included in the proposed model (3).

$$\min_{X_{\mathrm{rlt}},Y_{\mathrm{rlt}},R_{\mathrm{rlt}}} \sum_{i_1} \left\{ \left\| \begin{bmatrix} \alpha_{\mathrm{rlt}} & 0 & 0 \\ 0 & \beta_{\mathrm{rlt}} & 0 \end{bmatrix} {}^{\mathrm{lt}}P_1(i_1,\mathrm{sgn}(\dot{\theta}^*_{1,\mathrm{map}}(i_1))) - \begin{bmatrix} X_{\mathrm{rlt}} \\ Y_{\mathrm{rlt}} \end{bmatrix} \right\| - R_{\mathrm{rlt}} \right\}^2 \tag{7}$$

$$\begin{bmatrix} P_n(i_n,\mathrm{sgn}(\dot{\theta}^*_{n,\mathrm{map}}(i_n))) \\ 1 \end{bmatrix} = \begin{bmatrix} \cos\theta_{\mathrm{rlt}} & \sin\theta_{\mathrm{rlt}} & 0 & 0 \\ -\sin\theta_{\mathrm{rlt}} & \cos\theta_{\mathrm{rlt}} & 0 & 0 \\ 0 & 0 & 1 & 0 \\ 0 & 0 & 0 & 1 \end{bmatrix} \begin{bmatrix} 1 & 0 & -\beta_{\mathrm{rlt}} & -X_{\mathrm{rlt}} \\ 0 & 1 & \alpha_{\mathrm{rlt}} & -Y_{\mathrm{rlt}} \\ \beta_{\mathrm{rlt}} & -\alpha_{\mathrm{rlt}} & 1 & -z_0 \end{bmatrix} \begin{bmatrix} {}^{\mathrm{lt}}P_n(i_n,\mathrm{sgn}(\dot{\theta}^*_{n,\mathrm{map}}(i_n))) \\ 1 \end{bmatrix} \tag{8}$$

The objective of the present scheme is to identify the angular positioning deviation of J_n-axis, $\Delta\theta^*_{n,\mathrm{map}}(i_n,+1)$ and $\Delta\theta^*_{n,\mathrm{map}}(i_n,-1)$ for all $i_n = 1,\ldots,N_n$, and for both axes, $n = 1,2$, as well as the D-H parameters, ΔL_1, ΔL_2 and θ_{20}. This paper proposes the following test using a laser tracker. Figure 2 illustrates the proposed test procedure. Figure 3 shows the experimental setup.

1. Keep the J_1-axis at $\theta^*_1 = 0°$. Index the J_2-axis at $\theta^*_{2,\mathrm{map}}(1),\ldots,\theta^*_{2,\mathrm{map}}(N_2)$. $\theta^*_{2,\mathrm{map}}(i_2)$ should be given bidirectionally. The range of $\theta^*_{2,\mathrm{map}}(i_2)$ should cover the J_2-axis rotation stroke as much as possible. At each stop position, the three-dimension (3D) position of the end effector is measured by using a laser tracker. Figure 2a shows the test setup.

2. Similarly, keeping the J_2-axis at $\theta^*_2 = 0°$. J_1-axis is indexed at $\theta^*_{1,\mathrm{map}}(1),\ldots,\theta^*_{1\mathrm{map}}(N_1)$. $\theta^*_{1,\mathrm{map}}(i_1)$ should also be given bidirectionally. The end effector 3D position at each stop point is also measured by using a laser tracker. Figure 2b shows the test setup.

2.4 Identification of bidirectional angular position deviation of each rotary axis

The end effector position measured in the proposed test in Section 2.3 is denoted by ${}^{\mathrm{lt}}P_n(i_n,\mathrm{sgn}(\dot{\theta}^*_{n,\mathrm{map}}(i_n))) \in \mathbb{R}^3(i_n = 1,\ldots,N_n)$, where J_n-axis is at the command angle $\theta^*_{n,\mathrm{map}}(i_n)$ and its rotation direction is represented by $\mathrm{sgn}(\dot{\theta}^*_{n,\mathrm{map}}(i_n))$ (either $+1$ or -1). The laser tracker has its own CS, and the left-hand side superscript "lt" represents a vector defined in the laser tracker CS. Figure 4 shows the overview of the proposed algorithms.

1. Conversion to the reference CS: as described in Section 2.1, the reference CS is defined such that its Z-axis is aligned to the J_1-axis average line. The angle of the J_1-axis average line to the Z-axis of the laser tracker CS around the X- and Y-axis, denoted by α_{rlt} and $\beta_{\mathrm{rlt}} \in \mathbb{R}$,
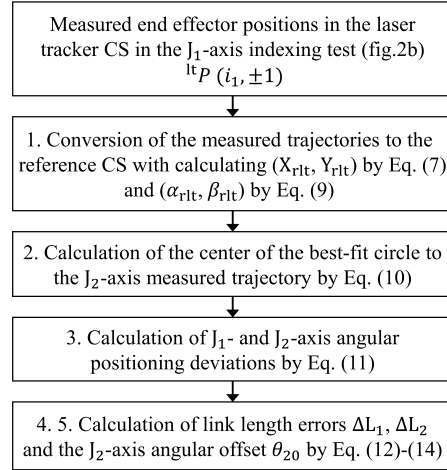
Fig. 4: Overview of the proposed algorithm

can be calculated by solving Eq. (9).

$$\min_{\substack{\alpha_{\mathrm{rlt}}, \\ \beta_{\mathrm{rlt}}, z_0}} \sum_{i_1} \{A - z_0\}^2$$
$$A = \begin{bmatrix} -\beta_{\mathrm{rlt}} & \alpha_{\mathrm{rlt}} & 0 \end{bmatrix} {}^{\mathrm{lt}}P_1(i_1,\mathrm{sgn}(\dot{\theta}^*_{1,\mathrm{map}}(i_1))) \tag{9}$$

where α_{rlt} and β_{rlt} are the inner product of a vector with $\begin{bmatrix} -\beta_{\mathrm{rlt}} & \alpha_{\mathrm{rlt}} & 0 \end{bmatrix}$ represents the Z position of the vector rotated by α_{rlt} around X and by β_{rlt} around Y. If this assumption is not met, Eq. (9) can be rewritten with the rotation matrices.

The (X, Y) position of the J_1-axis average line, projected onto the XY plane in the laser tracker CS, denoted by $(X_{\mathrm{rlt}}, Y_{\mathrm{rlt}})$, is given as the center of the best-fit circle of the measured trajectory rotated by α_{rlt} and β_{rlt}. It can be calculated by solving Eq. (7).

The X-axis of the reference CS is defined such that it passes the measured position when the J_1-axis is at its reference angular position, denoted by $\theta^*_{1,\mathrm{map}}(i_1^0)$.

Then, by using $\alpha_{\mathrm{rlt}}, \beta_{\mathrm{rlt}}, X_{\mathrm{rlt}}, Y_{\mathrm{rlt}}, \theta_{\mathrm{rlt}}$, and z_0 calculated in Eqs. (7) and (9), the measured end effector position in the laser tracker CS, can be converted to the reference CS by Eq. (8).

2. Calculate the center of the best-fit circle, denoted by $Q_2 \in \mathbb{R}^2$, to the measured trajectory with the J_2-axis indexing test, $P_2(i_2, \mathrm{sgn}(\dot{\theta}^*_{2,\mathrm{map}}(i_2)))$ $(i_2 = 1, \ldots, N_2)$, and the radius, $R_2 \in \mathbb{R}$, by solving the problem in Eq. (10).

$$
\begin{aligned}
&\min_{Q_2,\,R_2} \sum_k \left\{ \left\| B - Q_2 \right\| - R_2 \right\}^2 \\
&B = \begin{bmatrix} 1 & 0 & 0 \\ 0 & 1 & 0 \end{bmatrix} P_2(i_2, \mathrm{sgn}(\dot{\theta}^*_{2,\mathrm{map}}(i_2)))
\end{aligned} \tag{10}
$$

3. The angle- and direction-dependent angular positioning deviation of J_n-axis, can be calculated by Eq. (11)

$$
\begin{aligned}
\Delta\theta^*_{n,\mathrm{map}}(i_n, \pm 1) = {}& \angle(P_n(i_n, \pm 1) - Q_n) \\
& - \angle(P_n(i_n^0, \pm 1) - Q_n) - \theta^*_{n,\mathrm{map}}(i_n)
\end{aligned} \tag{11}
$$

where $\theta^*_{n,\mathrm{map}}(i_n^0)$ is the reference angular position of J_n-axis (see Step Section 2.3). $\angle(P_n)$ denotes the angle between the vector $P_n \in \mathbb{R}^3$, projected onto the XY plane, and X-axis of the reference CS. Eq. (11) must be calculated for all $i_n = 1, \ldots, N_n$ bidirectionally. Note the $Q_1 = [0\ 0\ 0]^\mathrm{T}$ by the definition of the reference CS.

4. The length errors of the first and second links, ΔL_1 and ΔL_2, can be calculated by Eqs. (12) and (13).

$$
\Delta L_1 = R_{\mathrm{rlt}} - R_2 - L_1 \tag{12}
$$

$$
\Delta L_2 = R_2 - L_2 \tag{13}
$$

5. The angular offsets of J_2-axis, θ_{20}, can be calculated by Eq. (14).

$$
\theta_{20} = \angle(P_2(i_2^0, \mathrm{sgn}(\dot{\theta}^*_{2,\mathrm{map}}(i_2^0))) - Q_2) - \angle(Q_2 - Q_1) \tag{14}
$$

The D-H parameters, ΔL_1, ΔL_2, and θ_{20}, defines the position of the J_1- or J_2-axis average lines [38] . The axis average line, defined in [2], represents the mean position and orientation of the axis of rotation. The calculation of the D-H parameters by solving Eq. (10) complies with this definition of the D-H parameters.

3 Experiments to identify the error parameters in proposed model

3.1 Experiment setup

In this experiment, a SCARA-type robot, RH-3FRH-5515-D by Mitsubishi Electric Co., Ltd. was measured by a laser tracker, Leica's AT960-XR, as shown in Fig. 3. The major specifications of the robot are shown in Table 1. The cat's eye retroreflector is installed on the robot end effector to reflect the laser beam. The retroreflector is mounted on a screw-driven stage such that the center of the retroreflector can be roughly aligned to the centerline of J_4-axis (see Fig. 3). Table 2 shows the laser tracker's major specifications. In this experiment, the measured distance was about 2.8m by average. According to Table 2, the laser tracker's measurement uncertainty is about $\pm 30\,\mu\mathrm{m}$, by average. Throughout the experiment, the Z-position of the robot end effector was kept at $Z^* = 300\,\mathrm{mm}$ in the reference CS.

The measurement described in Section 2.3 was performed with the J_2- and J_1-axis command angular positions in Eq.s (15) and (16).

$$
\begin{aligned}
\theta^*_{2,\mathrm{map}}(i_2) = [&-143°, -140°, -130°, -120°, \ldots, \\
&140°, 143°] \in \mathbb{R}^{31}(i_2 = 1, \ldots, 31)
\end{aligned} \tag{15}
$$

Table 1: Major specifications of the robot (RH-3FRH-5515-D by Mitsubishi Electric Co., Ltd.)

| Nominal link lengths	Operating range	Position repeatability
L_1: 325mm	J_1-axis: 340°	X-Y composite: $\pm$0.012mm
L_2: 225mm	J_2-axis: 290°	J_3-axis: $\pm$0.01mm
	J_3-axis: 150mm	J_4-axis: $\pm$0.0004°
	J_4-axis: 720°	

Table 2: Major specifications of the laser tracker (Leica AT960-XR by Hexagon Manufacturing Intelligence)

Reflector Measuring range (diameter)	Horizontal measuring range	Vertical measuring range	Measurement accuracy U_{xyz}
160m	360°	$\pm$145°	$\pm 15\mu\mathrm{m} + 6\mu\mathrm{m/m}$
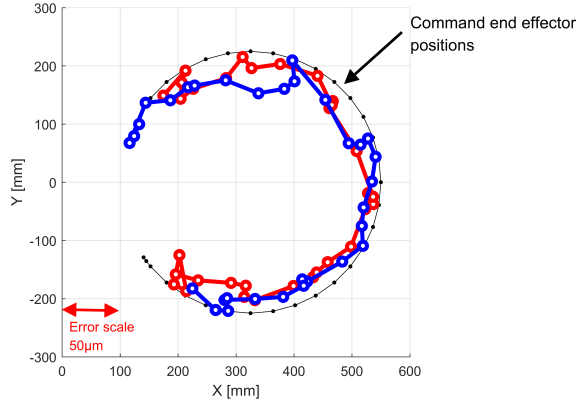
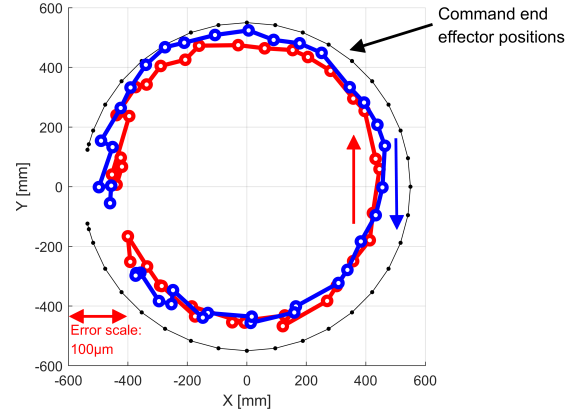**Fig. 5**: Measured end effector positions for J$_2$-axis command angles in Eq. (15)
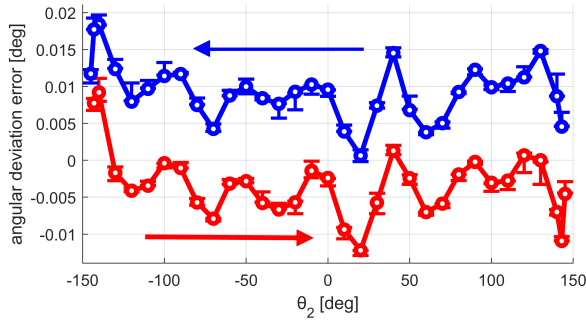
Fig. 6: Identified J$_2$-axis angular deviation $\Delta\theta^*_{2,\mathrm{map}}(i_2, \mathrm{sgn}(\dot{\theta}^*_2(i_2)))$

$$\theta^*_{1,\mathrm{map}}(i_1) = [-165°, -160°, -150°, -140°, \ldots,$$
$$160°, 165°] \in \mathbb{R}^{35}(i_2 = 1, \ldots, 35) \quad (16)$$

The black dots in Fig. 2 shows the end effector command positions, denoted by $P^*_1(i_1, \mathrm{sgn}(\dot{\theta}^*_{1,\mathrm{map}}(i_1)))$ and $P^*_2(i_2, \mathrm{sgn}(\dot{\theta}^*_{2,\mathrm{map}}(i_2)))$, given in Eq. (1) with command angular positions either in Eq. (15) or (16).

3.2 Identification of J$_1$-axis, J$_2$-axis angular positioning deviations

For the J$_2$-axis indexing test, described in Fig. 2a, the measured end effector positions are shown in Fig. 5. The test was repeated three times. Figure 5 shows only the data from the first measurement. The black dots represent the command end effector points, $P^*_2(i_2, \mathrm{sgn}(\dot{\theta}^*_{2,\mathrm{map}}(i_2)))$, and red and blue circles represent the measured positions, $P^*_n(i_n, \mathrm{sgn}(\dot{\theta}^*_{n,\mathrm{map}}(i_n)))$, as J$_2$-axis rotates in positive (counter-clockwise, in red circles) and negative (clockwise, in blue circles) directions. The

Fig. 7: Measured end effector positions for J$_1$-axis command angles in Eq. (16)
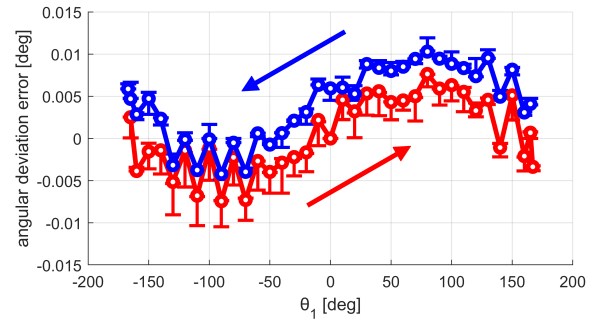
Fig. 8: Identified J$_1$-axis angular deviation $\Delta\theta^*_{1,\mathrm{map}}(i_1, \mathrm{sgn}(\dot{\theta}^*_1(i_1)))$

error from the command to measured positions is magnified 2,000 times ("Error scale" in Fig. 5 corresponds to the error 50 μm).

Throughout this paper, the end effector positions were statically measured. It was confirmed that static end effector positions in the robot controller, calculated from J$_1$- and J$_2$-axis angular positions, had negligibly small difference from the command positions.

Figure 6 shows the identified J$_2$-axis angular positioning deviations $\Delta\theta^*_{2,\mathrm{map}}(i_2, \mathrm{sgn}(\dot{\theta}^*_2(i_2)))$ at each command angle $\theta^*_{2,\mathrm{map}}(i_2)$ calculated by Eq. (11) with the first measured bidirectional trajectory shown in Fig. 5. The red polyline represents $\Delta\theta^*_{2,\mathrm{map}}(i_2, +1)$ when J$_2$-axis rotates in the positive direction. The blue polyline represents $\Delta\theta^*_{2,\mathrm{map}}(i_2, -1)$ when J$_2$-axis rotates in the negative direction. The difference between the identified angular positioning deviations in positive and negative directions represents the influence of the backlash in the J$_2$-axis. The error bar represents the maximum and minimum values in the three

measurements, which show the repeatability of J_2-axis angular positioning and the measurement.

The same calculation is applied to the J_1-axis indexing test. The measured end effector positions at $P_1^*(i_1, \text{sgn}(\dot{\theta}_{1,\text{map}}^*(i_1)))$ are shown in Fig. 7. Three tests were repeated, but Fig. 7 only shows the first m easurement d ata. Figure 8 shows the identified J $_1$-axis a ngular devia- tion $P_1^*(i_1, \text{sgn}(\dot{\theta}_{1,\text{map}}^*(i_1)))$ calculated by Eq. (11) based on the first measurement data. Table 3 shows the identified D-H parameters included in Eq. (3) calculated by Eqs. (12)-(14).

Remark 1: Figure 8 shows a sinusoidal com- ponent. This is not caused by identification error of the best-fit center, Q_2 in Eq. (10), but indeed shows the angular positioning deviation, since the radial error motion, shown in Fig. 14, is calcu- lated by using the same Q_2 but does not show a sinusoidal component.

Remark 2: According to the manufacturer's catalog, the measurement uncertainty of the laser tracker, shown in Table 2, may not be sufficiently small compared to the robot's positioning error, shown in Figs. 5, 7, and 9. However, the experi- mental results show that the repeatability of the measurement was sufficiently small compared to the robot's positioning error (see the error bars in Figs 6 and 8). Note that they also contain the influence of the robot's positioning repeata- bility. The measurement uncertainty of a laser tracker can be potentially a critical issue for higher accuracy positioning by a robot.

4 Experimental validation of prediction accuracy of the identified model

## 4.1 Verification of the prediction accuracy of the proposed kinematic model

To experimentally investigate the prediction accu- racy of the proposed kinematic model identified in Section 3.2, the measured and predicted paths were compared for the command paths shown by black dots ("●") in Fig. 9 (bidirectional). The end

Table 3: Identified D-H parameters

| ΔL_1(mm)	$L_1 + \Delta L_1$(mm)	ΔL_2(mm)	$L_2 + \Delta L_2$(mm)	θ_{20}(deg)
-0.0347	324.9650	-0.0178	224.9832	-0.0032
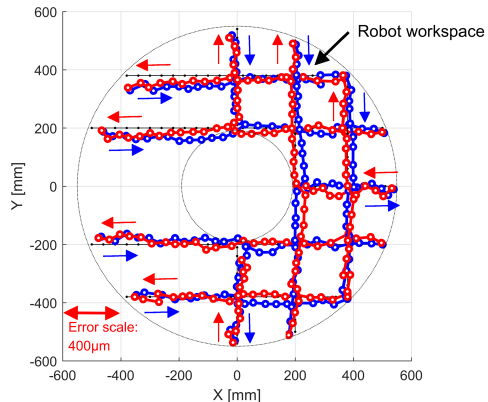
Fig. 9: 2D positioning error measured by the laser tracker
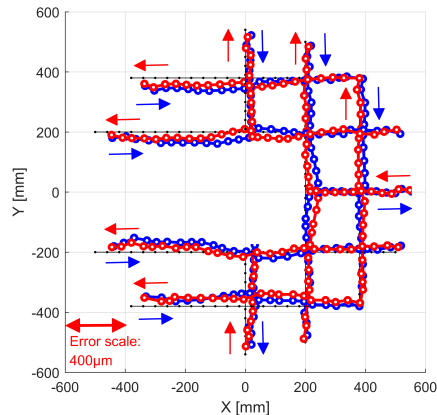

Fig. 10: 2D positioning error estimated by the proposed model

effector positions in the reference CS, measured by the same laser tracker, are shown in Fig. 9 by red and blue circles (" ○" and "○") for the feed direc- tion shown by red and blue arrows. The error from the command to measured positions is magnified 500 times ("Error scale" in Figs. 9−12 corresponds to the error 400μm).

Then, the 2D positioning error is predicted by using the proposed kinematic model at each of the same command positions. The predicted end effector positions are shown in Fig. 10. Compared with the measured positions in Fig. 9, it shows a good match. This shows the proposed kinematic model's prediction accuracy, even though the sim- ulated paths are completely different from the paths used in the model identification (see Fig. 2). Figure 9 shows that the 2D contour error is signif- icantly different for different feed directions (the difference between the blue and red paths is about 80 μm at maximum). This is mostly attributable
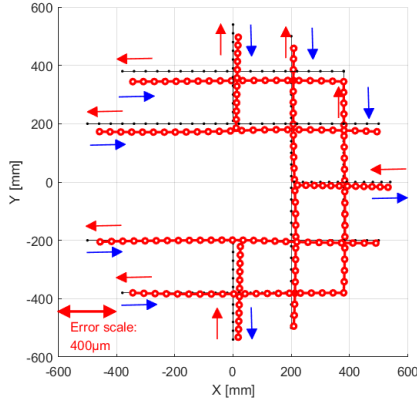
**Fig. 11**: 2D positioning error estimated by the conventional model
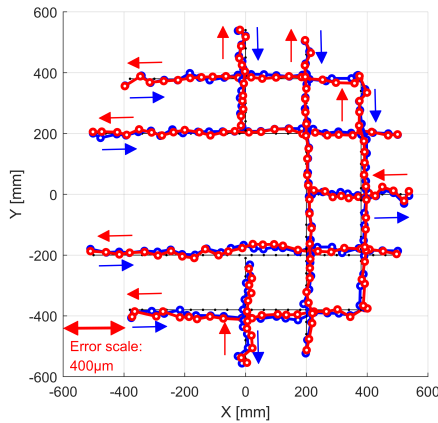
Fig. 12: Measured end effector positions under the compensation based on the proposed model

to the rotary axis backlash, and Fig. 10 shows that the identified model can predict its influence with sufficient accuracy. For the comparison, Fig. 11 shows the end effector positions predicted by the conventional model, given in Eq. (2), with the D-H paramenters identified in Table 3. It shows that the conventional model's estimation accuracy is significantly lower than the proposed model. The conventional model cannot distinguish the positioning error in different feed directions.

4.2 Compensation for the end effector positioning error

This paper uses a straightforward off-line method to compensate the robot positioning error. The predicted robot end effector position, $\hat{P}(k)$, based on the proposed kinematic model ((3)) is inverted relative to the command end effector position, $P^*(k)$, and the inverted coordinate position is used
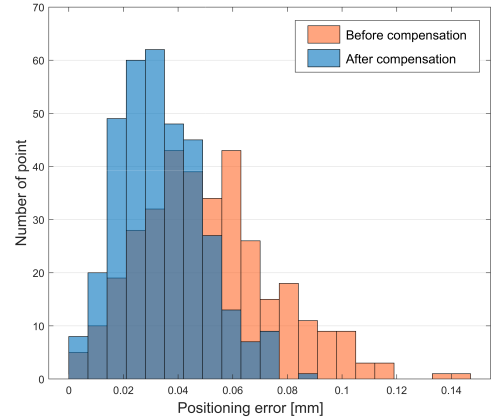
Fig. 13: Absolute position error distribution of measurement points

as the compensated position. The compensated position, $P^*_{\mathrm{com}}(k) \in \mathbb{R}^2$, is calculated by Eq. (17).

$$P^*_{\mathrm{com}}(k) = P^*(k) - (\hat{P}(k) - P^*(k)) \qquad (17)$$

For the compaensated trajectories, the end effector position was measured by using a laser tracker. Figure 12 shows the bidirectional trajectories with this compensation. Compared to Fig. 9, Fig. 12 shows that the new kinematic model can effectively improve the absolute positioning accuracy over the entire workspace. In particular, the impact of the rotary axis backlash is significantly reduced in Fig. 12.

Figure 13 compares the absolute positioning errors of all measurement points before and after compensation. The average positioning error before compensation was 0.051 mm, and 0.034 mm after compensation. By the compensation, the absolute positioning error of the robot was reduced by 33%.

5 Extension of the proposed model

For machine tool, ISO 230-7[9] describes test procedures to measure all the error motions of a rotary axis. In addition to the angular positioning error motion, the axis of rotation may be displaced or tilted as it rotates. Such error motions are called the radial and tilt error motions. Naturally, a rotary axis in a robot can also have radial and tilt error motions. This paper so far only considers the angular positioning error motion, since it often has a larger influence on the end effector positioning accuracy, but the present modelling

scheme can be extended to other error motions in a straightforward manner.

A machine tool often has one rotary axis mounted on another rotary axis. In such a configuration, error motions of one rotary axis may be influenced by the angular position of the other rotary axis. For example, Ibaraki et al. [39] discusses such an influence for a rotary table (C'-axis) mounted on a swivel axis (B'-axis). When the swivel axis is horizontal ($B = 0°$) and vertical ($B = \pm90°$), the error motion of the rotary table (C-axis) may significantly change, due to the deformation of the C-axis bearing caused by the gravity to the rotary table. Such an axis-to-axis accuracy cross-talk can exist also on a robot. The modelling scheme presented in this paper can be extended to model such an influence.

Unlike machine tools, such an influence on the positioning accuracy of an industrial robot has not been discussed in the literature. To illustrate the extensibility of the present scheme to a wider class of error motions, this section will present three examples of such an analysis of experimental results.

5.1 Radial error motion of rotary axes

5.1.1 Inclusion of radial error motion of rotary axis into the kinematic model

The geometric inaccuracy (the roundness error) of the bearing laces is often a major cause for the radial error motion of a rotary axis. The movement of bearing balls, as well as the gear teeth, can cause the radial error motion typically in a periodic form of the frequency corresponding to the ball pitch or the gear pitch[40]. When the disturbance is dependent on the angular position, for example, when the gravity influence changes with the angular position, then it can cause the radial error motion that changes with the angular position. *Radial error motion*, the term in [9], is defined as error motion that occurs perpendicular to the rotary axis of rotation at a specified axial location. Similarly as the angular positioning error motion, the radial error motion is generally a function of the angular position.

Such a radial error motion influence can be incorporated into the proposed model. Denote the radial error motion at the command angular position, $\dot{\theta}_{n,\mathrm{map}}^*(i_n)$, by $E_{\mathrm{radial},n,\mathrm{map}}(i_n, \mathrm{sgn}(\dot{\theta}_n^*(k)))$. Similar as the angular positioning error motion, the radial error motion is modelled as a function

of the rotation direction, $\mathrm{sgn}(\dot{\theta}_n^*(k))$. Then, with this radial error motion, the proposed kinematic model (3) is modified as Eq. (18),

$$\hat{P}(k) = \begin{bmatrix} \cos\hat{\theta}_1(k) & \cos(\hat{\theta}_1(k) + \hat{\theta}_2(k) + \theta_{20}) \\ \sin\hat{\theta}_1(k) & \sin(\hat{\theta}_1(k) + \hat{\theta}_2(k) + \theta_{20}) \end{bmatrix}$$
$$\begin{bmatrix} L_1 + \Delta L_1 + E_{\mathrm{radial},1}(k, \mathrm{sgn}(\dot{\theta}_1^*(k))) \\ L_2 + \Delta L_2 + E_{\mathrm{radial},2}(k, \mathrm{sgn}(\dot{\theta}_2^*(k))) \end{bmatrix} \quad (18)$$

where $E_{\mathrm{radial},n}(k, \mathrm{sgn}(\dot{\theta}_n^*(k)))$, represents the radial error motion at the arbitrary command angular position, $\dot{\theta}_n^*(k)$. According to the definition of the term "radial error motion" in [2], it is defined such that its mean is zero. It is given by linearly interpolating $E_{\mathrm{radial},n,\mathrm{map}}(i_n, \mathrm{sgn}(\dot{\theta}_n^*(k)))$ ($n = 1, 2$), similarly as the angular positioning deviation, as Eq. (19).

$$E_{\mathrm{radial},n}(k, \mathrm{sgn}(\dot{\theta}_n^*(k)))$$
$$= \delta_1(k) \cdot E_{\mathrm{radial},n,\mathrm{map}}(i_n, \mathrm{sgn}(\dot{\theta}_n^*(k)))$$
$$+ (1 - \delta_1(k)) \cdot E_{\mathrm{radial},n,\mathrm{map}}(i_n + 1, \mathrm{sgn}(\dot{\theta}_n^*(k)))$$
$$(19)$$

$\delta_n(k)$ is defined in Eq. (6). Other error parameters, ΔL_n, $\hat{\theta}_n(k)$, are identified in Section 2.2.

### 5.1.2 Identification of radial error motions and experiment

The same test procedure presented in Section 2.3 is applied to identify the radial error motion, denoted by $E_{\mathrm{radial},n,\mathrm{map}}(i_n, \mathrm{sgn}(\dot{\theta}_n^*(i_n))) \in \mathbb{R}$ ($n = 1, 2$). It can be calculated by Eq. (20).

$$E_{\mathrm{radial},n,\mathrm{map}}(i_n, \mathrm{sgn}(\dot{\theta}_n^*(k)))$$
$$= \left\| P_n(i_n, \mathrm{sgn}(\dot{\theta}_{n,\mathrm{map}}^*(i_n))) - Q_n \right\| \quad (20)$$

where $P_n(i_n, \mathrm{sgn}(\dot{\theta}_{n,\mathrm{map}}^*(i_n)))$ represents the measured end effector positions in the J_n-axis indexing test given in the reference CS as shown in Eq. (8). Q_n represents the center position of the best-fit circle to the measured trajectory and its definition is given in Eq. (10).

From the measured end effector positions shown in Figs. 5 and 7, the radial error motion, $E_{\mathrm{radial},n,\mathrm{map}}(i_n, \mathrm{sgn}(\dot{\theta}_n^*(k)))$, is calculated. Figures 14 and 15 show the identified $E_{\mathrm{radial},n,\mathrm{map}}(i_n, \mathrm{sgn}(\dot{\theta}_n^*(k)))$.
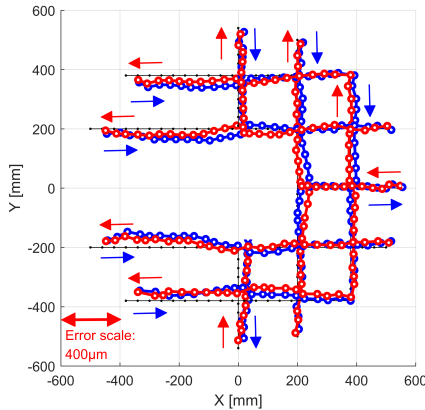
Then, for the same command paths shown in black dots in Fig. 9, Fig. 16 shows the predicted
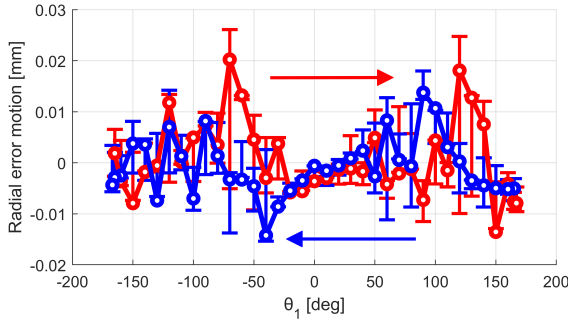
Fig. 14: Identified J_1-axis radial error motion $E_{\mathrm{radial},1,\mathrm{map}}(i_1, \mathrm{sgn}(\dot{\theta}_1^*(i_1)))$
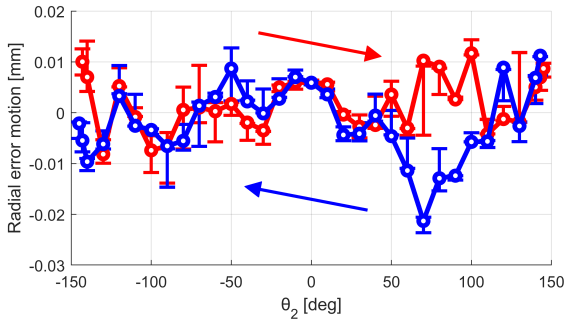

Fig. 15: Identified J_2-axis radial error motion $E_{\mathrm{radial},2,\mathrm{map}}(i_2, \mathrm{sgn}(\dot{\theta}_2^*(i_2)))$

Fig. 16: 2D positioning error estimated by the proposed model added radial error motion

trajectories of the model (18) with J_1- and J_2-axis radial error motions (Figs 14 and 15) , in addition to the J_1- and J_2-axis angular positioning deviations (Figs. 6 and 8) and the D-H parameters (Table 3) identified in Section 3.2. Comparing Fig. 16 and Fig. 10, it can be found that, in this particular robot, the radial error motions do not have significant influence on the predicted results. The estimated radial error motions, shown in Figs. 14
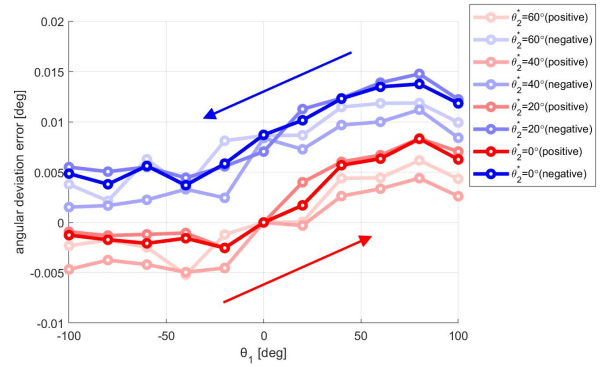
Fig. 17: J_1-axis angular positioning deviation at diffident J_2-axis angles

and 15, are relatively smaller than the positioning error observed in Fig. 9.

For this particular robot, the radial error motions, shown in Figs. 14 and 15, were not significant. While the radial error motion of a spindle can be easily measured by using, for example, a cylindrical artefact and a dial gauge [1], the radial error motion of a robot rotary axis is more difficult to measure, since it is typically difficult to place an artefact on its axis of rotation. This subsection presented a scheme to measure it. This is a contribution of this subsection.

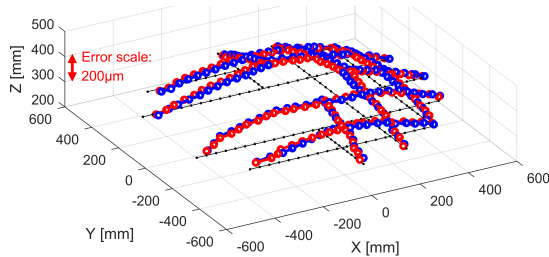## 5.2 Axis-to-axis cross-talk in angular positioning deviation

5.2.1 Possible cause for axis-to-axis cross-talk in angular positioning deviation

In the proposed model in Eq. (3), the angular positioning deviation of a rotary axis is assumed dependent only on its command angle and rotating direction. In the proposed model in Eq. (3), the angular positioning deviation of a rotary axis is assumed dependent only on its command angle and rotating direction. The axis-to-axis cross talk can be incorporated into the proposed model by making the angular positioning deviation of J_1-axis dependent not only the J_1 angular position but also on the J_2 angular position.

For the SCARA robot configuration in Fig. 1, the gravity influence as a static torque to the J_1-axis is clearly maximized when $\theta_2^* = 0°$ (the pose shown in Fig. (1)). As θ_2^* increases (or decreases), the center of gravity of the robot will move towards the J_1-axis, and the influence of gravity will decrease. Therefore, the following sub-section will investigate the influence of the J_2-axis
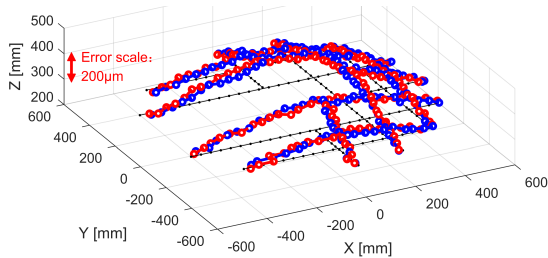
Fig. 18: 3D end effector positioning errors measured by the laser tracker

Fig. 19: 3D end effector positioning errors estimated by the proposed model (23)

angular position on the J_1-axis angular positioning error motion.

5.2.2 Identification of axis-to-axis cross-talk in angular positioning deviation and experiment

For identifying the influence of the J_2-axis angular position on the angular positioning deviation of J_1-axis, the following test procedure is proposed:

1. Keep the J_2-axis at $\theta_2^* = 0°$. Index the J_1-axis as shown in Eq. (21).

$$\theta_{1,\mathrm{map}}^*(i_1) = \\ [-100°, -80°, -60°, -40°, \ldots, 80°, 100°] \\ \in \mathbb{R}^{11} (i_1 = 1, \ldots, 11) \quad (21)$$

$\theta_{1,\mathrm{map}}^*(i_1)$ should be given bidirectionally. At each stop position, the 3D position of the end effector is measured by using a laser tracker.

2. Keep the J_2-axis at $\theta_2^* = 20°, 40°, 60°$. At each J_2-axis angular position, perform Step 1.

For each J_1-axis angular position, the J_1-axis angular positioning deviations is identified by Eq. (11). Figure 17 compares the J_1-axis angular positioning deviations identified at $\theta_2^* = 20°, 40°, 60°$. The difference is not significant, compared to the robot's unrepeatable positioning error (see error bars in Fig. 8), or the measurement uncertainty

of the laser tracker. The present test results show that, in this particular robot, the influence of the J_2-axis angular position on the J_1-axis angular positioning deviation is not significant.

If such influences are significant, the present model can be straightforwardly extended to include the J_1-axis angular positioning deviation that is dependent on not only the J_1-axis angular position but also on the J_2-axis angular position. This represents the axis-to-axis cross-talk in the J_1-axis angular positioning deviation.

5.3 Parallelism errors of J_2- to J_1-average line

In the proposed model in Eq. (3), only 2D positioning error was estimated. On a typical SCARA robot, the positioning error in the Z-direction is often significantly influenced by error motions of the Z-axis (J_4-axis in Fig. 1). In many SCARA robots, a linear Z-axis is often not designed for higher positioning accuracy (for example, it often has no linear guideway). Therefore, this paper so far does not consider the positioning error in the Z-directions. However, when needed, it is straightforward to extend the present model to the 3D positioning. This section demonstrates the inclusion of the *parallelism errors* (the term in [2]) of J_1- to J_2-axis average lines into the present model to model the 3D positioning error in the entire workspace.

First, Fig. 18 shows the 3D positions of the end effector measured for the command paths shown by black dots in Fig. 9. It show significant positioning errors in the Z-direction. The parallelism error of J_2- to J_1-axis average lines is considered to be its major cause. For industrial robots, the parallelism error of axes may be caused by assembly errors. The parallelism errors of J_2- to J_1-axis around X- and Y-axes, denoted respectively by $E_{A(0J_1)J_2}$ and $E_{B(0J_1)J_2}$, can be identified by the following procedure: perform the J_2-axis indexing test, described in Step 1 of Section 2.3. From the measured 3D end effector positions, $P_2^*(i_2, \mathrm{sgn}(\dot{\theta}_{2,\mathrm{map}}^*(i_2)))$, $E_{A(0J_1)J_2}$, and $E_{B(0J_1)J_2}$ can be identified by solving Eq. (22).

Table 4: Identified parallelism errors of J_2- to J_1-axis

$E_{A(0J_1)J_2}$ (deg)	$E_{B(0J_1)J_2}$ (deg)	z_1 (mm)
-0.0009	0.0293	-0.2715

$$\min_{E_{\text{A}(0\text{J}_1)\text{J}_2}, E_{\text{B}(0\text{J}_1)\text{J}_2}, z_1} \sum_{i_2} \left\{ \begin{bmatrix} E_{\text{A}(0\text{J}_1)\text{J}_2} & E_{\text{B}(0\text{J}_1)\text{J}_2} & 0 \end{bmatrix} P_2(i_2, \text{sgn}(\dot{\theta}_{2,\text{map}}^*(i_2))) - z_1 \right\}^2 \tag{22}$$

$$\hat{P}(k) = \begin{bmatrix} (L_1 + \Delta L_1)\cos(\hat{\theta}_1(k)) + (L_2 + \Delta L_2)\cos(\hat{\theta}_1(k) + \hat{\theta}_2(k) + \theta_{20}) \\ (L_1 + \Delta L_1)\sin(\hat{\theta}_1(k)) + (L_2 + \Delta L_2)\sin(\hat{\theta}_1(k) + \hat{\theta}_2(k) + \theta_{20}) \\ (L_2 + \Delta L_2) \cdot (E_{\text{A}(0\text{J}_1)\text{J}_2})\sin(\hat{\theta}_2(k) + \theta_{20}) - E_{\text{B}(0\text{J}_1)\text{J}_2}\cos(\hat{\theta}_2(k) + \theta_{20}) \end{bmatrix} \tag{23}$$

The calculation results are shown in Table 4. The influence of the parallelism errors on the positioning error in the XY plane is negligibly small, when there is no command movement to the Z-direction. The proposed kinematic model (3) is extended to Eq. (23).

For the same command paths in Fig. 18, the positioning errors estimated by the model in Eq. (23) are shown in Fig. 19. Figures 18 and 19 show a good match, which indicates that the parallelism errors are the main cause for the Z-position error. It is emphasized that the parallelism errors were not identified by the measured trajectories in Fig. 18, but by the tests shown in Fig. 2.

6 Conclusion

For offline compensation of a robot's "absolute" positioning error over its entire workspace, the prediction accuracy of the robot's kinematic model is a key. Most of conventional works employ a kinematic model with position and orientation errors of rotary axis average lines, called the D-H parameters. Although they are clearly dominant error causes, they alone cannot exhibit sufficient prediction accuracy of the robot's positioning error. This was shown by experimental comparison with the measured end effector trajectories in Fig. 11.

Motivated with the volumetric error compensation for machine tools, this paper proposes a kinematic model for a SCARA-type robot with the angular positioning deviation of each rotary axis. The angular positioning deviation is modelled as a function of the command angular position, and a function of the rotation direction to model the backlash influence.

To identify the bidirectional angular positioning deviations, this research used a laser tracker to measure the position of the end effector when each joint is independently indexed at the given command angles. The comparison of the predicted end effector positions with the measured ones, for the paths that are completely different from the paths used for model identification, shows that the proposed kinematic model can accurately predict

the 2D position error. Furthermore, the compensation test was performed to cancel the predicted 2D positioning error, and the test results showed that it can improve the absolute position accuracy of the robot.

In addition, this study also demonstrates that the present model can be extended to include 1) radial rotation motion of each rotary axis, 2) axis-to-axis cross-talk in angular positioning deviation, and 3) the parallelism errors of J_2- to J_1-axis to model the 3D positioning error. The test results showed that the influence of 1) and 2) was not significant, but they showed potential applicability of the extended model to numerical compensation.

Declarations

Competing interests: The authors declare no competing interests.
Availability of data and material: The data and material that support the findings of this study are available on request.
Code availability: Not applicable.
Ethics approval: Not applicable.
Consent to participate: Written informed consent for publication was obtained from all participants.
Consent for publication: Written informed consent for publication was obtained from all participants.
Authors' contributions: These authors contributed equally to this work.

References

[1] Lee HM, Kim JB (2013) A Survey on Robot Teaching: Categorization and Brief Review. Applied Mechanics and Materials 330:648-656, https://doi.org/2013.10.4028/www.scientific.net/AMM.330.648

[2] ISO 230-1: 2012 (2012) Test code for machine tools - Part 1 : Geometric accuracy of machines operating under no-load

[3] Verl A, Valente A, Melkote S, et al (2019) Robots in machining. CIRP Annals 68:799-822. https://doi.org/10.1016/j.cirp.2019.05.009

[4] Chen Y, Dong F (2013) Robot machining: Recent development and future research issues. International Journal of Advanced Manufacturing Technology 66:1489-1497. https://doi.org/10.1007/

s00170-012-4433-4

[5] Uriarte L, Zatarain M, Axinte D, et al (2013) Machine tools for large parts. CIRP Annals - Manufacturing Technology 62:731-750. https://doi.org/10.1016/j.cirp.2013.05.009

[6] Bhatt PM, Malhan RK, Shembekar AV, et al (2020) Expanding capabilities of additive manufacturing through use of robotics technologies: A survey. https://doi.org/10.1016/j.addma.2019.100933

[7] Lakhal O, Chettibi T, Belarouci A, et al (2020) Robotized additive manufacturing of funicular architectural geometries based on building materials. IEEE/ASME Transactions on Mechatronics 25:2387-2397. https://doi.org/10.1109/TMECH.2020.2974057

[8] Chromy A (2015) High-accuracy volumetric measurements of soft tissues using robotic 3D scanner. IFAC-PapersOnLine 28:318-323. https://doi.org/10.1016/j.ifacol.2015.07.054

[9] ISO 230-7: 2015 (2015) Test code for machine tools - Part 7 : Geometric accuracy of axes of rotation

[10] Meggiolaro MA, Scriffignano G, Dubowsky S (2000) Manipulator Calibration Using a Single Endpoint Contact Constraint. International Design Engineering Technical Conferences and Computers and Information in Engineering Conference 35173:759-767. https://doi.org/10.1115/DETC2000/MECH-14129

[11] Bettahar H, Lehmann O, Clévy C, et al (2020) Photo-robotic extrinsic parameters calibration of 6-dof robot for high positioning accuracy. IEEE/ASME Transactions on Mechatronics 25:616-626. https://doi.org/10.1109/TMECH.2020.2965255

[12] Heping Chen, Fuhlbrigge T, Sang Choi, et al (2008) Practical industrial robot zero offset calibration. IEEE International Conference on Automation Science and Engineering 2008:516-521. https://doi.org/10.1109/COASE.2008.4626417

[13] Liu Y, Shi D, Ding J (2014) An automated method to calibrate industrial robot kinematic parameters using Spherical Surface constraint approach. The 4th Annual IEEE International Conference on Cyber Technology in Automation, Control and Intelligent 2014:365-370. https://doi.org/10.1109/CYBER.2014.6917491

[14] Joubair A, Bonev IA (2015) Kinematic calibration of a six-axis serial robot using distance and sphere constraints. International Journal of Advanced Manufacturing Technology 77:515-523. https://doi.org/10.1007/s00170-014-6448-5

[15] Cai Y, Gu H, Li C, et al (2017) Easy industrial robot cell coordinates calibration with touch panel. Robotics and Computer-Integrated Manufacturing 50:276-285. https://doi.org/10.1016/j.rcim.2017.10.004

[16] Nubiola A, Bonev IA (2013) Absolute calibration of an ABB IRB 1600 robot using a laser tracker. Robotics and Computer-Integrated Manufacturing 29:236-245. https://doi.org/10.1016/j.rcim.2012.06.004

[17] Nubiola A, Slamani M, Joubair A, et al (2014) Comparison of two calibration methods for a small industrial robot based on an optical CMM and a laser tracker. Robotica 32:447-466. https://doi.org/10.1017/S0263574713000714

[18] Švaco M, Šekoranja B, Šuligoj F, et al (2014) Calibration of an industrial robot using a stereo vision system. Procedia Engineering 69:459-463. https://doi.org/10.1016/j.proeng.2014.03.012

[19] Zhang X, Song Y, Yang Y, et al (2017) Stereo vision based autonomous robot calibration. Robotics and Autonomous Systems 93:43-51. https://doi.org/10.1016/j.robot.2017.04.001

[20] Filion A, Joubair A, Tahan AS, et al (2018) Robot calibration using a portable photogrammetry system. Robotics and Computer-Integrated Manufacturing 49:1339-1351. https://doi.org/10.1016/j.rcim.2017.05.004

[21] Hong C, Ibaraki S, Matsubara A (2011) Influence of position-dependent geometric errors of rotary axes on a machining test of cone frustum by five-axis machine tools. Precision Engineering 35:1-11. https://doi.org/10.1016/j.precisioneng.2010.09.004

[22] Lee K, Choi J, Bang Y (2016) Shaft position measurement using dual absolute encoders. Sensors and Actuators A: Physical 238:276-281. https://doi.org/10.1016/j.sna.2015.12.027

[23] Wu Y, Klimchik A, Caro S, et al (2015) Geometric calibration of industrial robots using enhanced partial pose measurements and design of experiments. Robotics and Computer-Integrated Manufacturing 35:151-168. https://doi.org/10.1016/j.rcim.2015.03.007

[24] Ibaraki S, Theissen NA, Archenti A, et al (2021) Evaluation of Kinematic and Compliance Calibration of Serial Articulated Industrial Manipulators. International Journal of Automation Technology 15:567-580. https://doi.org/10.20965/ijat.2021.p0567

[25] Zhuang H, Wu J, Huang W (1997) Optimal planning of robot calibration experiments by genetic algorithms. Journal of Robotic Systems 14:741-752. https://doi.org/10.1002/(SICI)1097-4563(199710)14:10⟨741::AID-ROB4⟩3.0.CO;2-U

[26] Zhao G, Zhang P, Ma G, et al (2019) System identification of the nonlinear residual errors of an industrial robot using massive measurements. Robotics and Computer-Integrated Manufacturing 59:104-114. https://doi.org/10.1016/j.rcim.2019.03.007

[27] Chen D, Li S, Liao L (2019) A recurrent neural network applied to optimal motion control of mobile robots with physical constraints. Applied Soft Computing 85:105880. https://doi.org/10.1016/j.asoc.2019.105880

[28] Slamani M, Nubiola A, Bonev IA (2012) Modeling and assessment of the backlash error of an industrial robot. Robotica 30:1167-1175. https://doi.org/10.1017/S0263574711001287

[29] Ruderman M, Hoffmann F, Bertram T (2009) Modeling and Identification of Elastic Robot Joints With Hysteresis and Backlash. IEEE Transactions on Industrial Electronics 56:3840-3847. https://doi.org/10.1109/TIE.2009.2015752

[30] Hörler P, Kronig L, Kneib JP, et al (2018) High density fiber postitioner system for massive spectroscopic surveys. Monthly Notices of the Royal Astronomical Society 481:3070-3082. https://doi.org/10.1093/mnras/sty2442

[31] Ayala HVH, dos Santos Coelho L (2012) Tuning of PID controller based on a multiobjective genetic algorithm applied to a robotic manipulator. Expert Systems with Applications, 39:8968-8974. https://doi.org/10.1016/j.eswa.2012.02.027

[32] Pierezan J, Freire RZ, Weihmann L, et al. (2017) Static force capability optimization of humanoids robots based on modified self-adaptive differential evolution Computers & Operations Research 84:205-215. https://doi.org/10.1016/j.cor.2016.10.011

[33] Mesmer P, Neubauer M, Lechler A, et al. (2022) Robust design of independent joint control of industrial robots with secondary encoders. Robotics and Computer-Integrated Manufacturing 73: 102232. https://doi.org/10.1016/j.rcim.2021.102232

[34] Cvitanic T, Melkote SN (2022) A new method for closed-loop stability prediction in industrial robots. Robotics and Computer-Integrated Manufacturing 73:102218. https://doi.org/10.1016/j.rcim.2021.102218

[35] Usui R, Ibaraki S (2022) A novel error mapping of bi-directional angular positioning devation of rotary axes in a SCARA-robot by "open-loop" tracking interferometer measurement. Precision Engineering 74:60-68. https://doi.org/10.1016/j.precisioneng.2021.11.002

[36] Kawano K, Ibaraki S (2020) Estimation of thermal influence on 2D positioning error of a SCARA-type robot over the entire workspace. The 18th International Conference on Precision Engineering:C-3-2

[37] Denavit J, Hartenberg R S (1955) A kinematic notation for lower-pair mechanisms based on matrices.

[38] Alam MM, Ibaraki S, Fukuda K (2021) Kinematic Modeling of Six-Axis Industrial Robot and its Parameter Identification: A Tutorial. International Journal of Automation Technology 15:599-610. https://doi.org/10.20965/ijat.2021.p0599

[39] Ibaraki S, Oyama C, Otsubo H (2011) Construction of an error map of rotary axes on a five-axis machining center by static R-test. International Journal of Machine Tools and Manufacture 51:190-200. https://doi.org/10.1016/j.ijmachtools.2010.11.011

[40] Cappa S, Reynaerts D, Al-Bender F(2014)Reducing the radial error motion of an aerostatic journal bearing to a nanometre level: theoretical modelling. Tribology Letters 53: 27-41. https://doi.org/10.1007/s11249-013-0241-8